JACS
JOURNAL OF THE AMERICAN CHEMICAL SOCIETY
Article
pubs.acs.org/JACS

Giant Ising-Type Magnetic Anisotropy in Trigonal Bipyramidal Ni(II) Complexes: Experiment and Theory

Renaud Ruamps,[†] Rémi Maurice,[†,‡,§] Luke Batchelor,[∥] Martial Boggio-Pasqua,[†] Régis Guillot,[∥] Anne Laure Barra,[⊥] Junjie Liu,[#] El-Eulmi Bendeif,[○,◆] Sébastien Pillet,[○,◆] Stephen Hill,*[,#,▽] Talal Mallah,*[,∥] and Nathalie Guihéry*[,†]

[†]Laboratoire de Chimie et Physique Quantiques, Université de Toulouse 3, 118 route de Narbonne, 31062 Toulouse cedex 06, France
[‡]Department of Theoretical Chemistry, Zernike Institute for Advanced Materials, University of Groningen, The Netherlands
[§]Departament de Química Física i Inorganica, Universitat Rovira i Virgili, Marcel.lí Domingo s/n, 43007 Tarragona, Spain
[∥]Université Paris Sud 11, CNRS, Institut de Chimie Moléculaire et des Matériaux d'Orsay, F-91405 Orsay, France
[⊥]Laboratoire National des Champs Magnétiques Intenses, UPR CNRS 3228, Université J. Fourier, 25, Avenue des Martyrs, B.P. 166, 38042 Grenoble Cedex 9, France
[#]National High Magnetic Field Laboratory, Florida State University, Tallahassee, Florida 32310, United States
[▽]Department of Physics, Florida State University, Tallahassee, Florida 32306, United States
[○]Université de Lorraine, CRM2, UMR 7036, Boulevard des Aiguillettes, Vandoeuvre les Nancy, F-54506, France
[◆]CNRS, CRM2, UMR 7036, Boulevard des Aiguillettes, Vandoeuvre les Nancy, F-54506, France

Supporting Information

ABSTRACT: This paper reports the experimental and theoretical investigations of two trigonal bipyramidal Ni(II) complexes, [Ni(Me_6tren)Cl]-(ClO_4) (**1**) and [Ni(Me_6tren)Br](Br) (**2**). High-field, high-frequency electron paramagnetic resonance spectroscopy performed on a single crystal of **1** shows a giant uniaxial magnetic anisotropy with an experimental D_{expt} value (energy difference between the $M_s = \pm 1$ and $M_s = 0$ components of the ground spin state S = 1) estimated to be between −120 and −180 cm^{-1}. The theoretical study shows that, for an ideally trigonal Ni(II) complex, the orbital degeneracy leads to a first-order spin−orbit coupling that results in a splitting of the $M_s = \pm 1$ and $M_s = 0$ components of approximately −600 cm^{-1}. Despite the Jahn−Teller distortion that removes the ground term degeneracy and reduces the effects of the first-order spin−orbit interaction, the D value remains very large. A good agreement between theoretical and experimental results (theoretical D_{theor} between −100 and −200 cm^{-1}) is obtained.

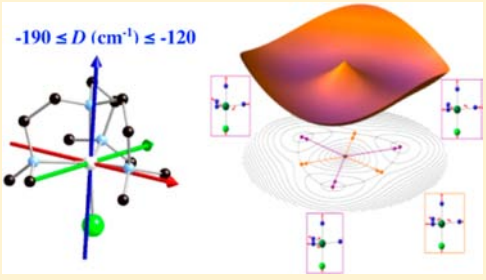

1. INTRODUCTION

Single molecule magnets (SMMs) exhibit a slow relaxation of their magnetization leading to a magnetic hysteresis at low temperature.[1−5] Since this bistable behavior may ultimately lead to technological applications in the domain of data storage[6] and quantum computing,[7−9] the study of these objects has generated a considerable interest. This remarkable property arises from the existence of two ground states of different magnetization $+M_s$ and $-M_s$ separated by an energy barrier. Magnetic anisotropy is responsible for both the existence of the energy barrier and the tunneling between the different M_s components. Nevertheless, the presently measured blocking temperatures of SMMs (below which the system keeps its magnetization) are still too low for daily technological applications. The magnitude of the anisotropy and its nature (either axial or rhombic) control the barrier height and the tunneling. The design of suitable SMMs therefore rests on the ability to synthesize new objects with larger and uniaxial magnetic anisotropy, characterized by a strongly negative axial anisotropy parameter D and an as small as possible rhombic parameter E. The lifting of degeneracy of the different M_s components of the high-spin ground term S originates from the spin−orbit coupling (and to a lesser extent the spin−spin coupling) combined with a low symmetry. In most of the 3d metallic complexes, magnetic anisotropy arises from the coupling between a spatially nondegenerate electronic ground state with excited states. Since these couplings are usually small in comparison with the energy difference between the electronic ground state and the excited states, the resulting anisotropy is usually weak.

Several strategies have been developed in order to enlarge the magnetic anisotropy of molecular complexes. One of them consists in replacing the d transition metals by rare earths (4f)

Received: August 16, 2012
Published: January 24, 2013

   dx.doi.org/10.1021/ja308146e | J. Am. Chem. Soc. 2013, 135, 3017−3026

or actinides (5f) in order to benefit from the large spin−orbit coupling of heavy elements.[10−14] The present work uses an alternative strategy[15] in which the complexes exhibit a nearly orbitally degenerate ground term. In such complexes, the first-order spin−orbit coupling between the spatial configurations resulting from the different orbital fillings may induce a large splitting of the M_s components of the high-spin degenerate ground term. In the recent past, several Ni(II) mononuclear complexes presenting a large Ising-type magnetic anisotropy have been proposed.[16] However, most of the Ni(II) complexes have a geometry close to octahedral in which the angular momentum is quenched. For Ni(II) complexes, one possible way to take advantage of first-order spin−orbit coupling is to design complexes with a low symmetry for which the ground term is orbitally degenerate. The main goal of this paper is to propose and study theoretically and experimentally such complexes. It is worth noting that, for the degenerate ground state, a Jahn−Teller distortion occurs. Unfortunately, this distortion that removes the orbital degeneracy tends to minimize the effect of the first-order spin−orbit coupling, thus reducing the magnetic anisotropy.[17−24]

In this paper, we report the synthesis, the characterization, and the single-crystal high-field high-frequency electron paramagnetic resonance (HF-HFEPR) study of [Ni(Me_6tren)Cl]-(ClO_4) (**1**) and [Ni(Me_6tren)Br]Br (**2**) trigonal bipyramidal complexes. In order to analyze the competition between the antagonist effects of the spin−orbit coupling and the Jahn−Teller distortion[25−28] in these two complexes, we also perform a theoretical study. Since the first attempt to calculate the anisotropic parameters in 1998,[29] in the $H_2Ti(\mu\text{-}H)_2TiH_2$ complex, several theoretical methods have been developed to calculate the zero-field splitting (ZFS) parameters. The NRLMOL code,[30,31] which constitutes one of the first density functional theory (DFT) implementations, has successfully been applied to various SMMs.[32−38] In 2003, the spin−orbit state interaction (SOSI) method,[39,40] which treats the spin−orbit coupling (SOC) in the wave function theory (WFT)-based framework, was implemented in the MOLCAS code.[41] This method has shown to provide reliable ZFS parameters of transition-metal complexes for which the ZFS is dominated by the SOC contribution,[42−51] and the present work uses this SOSI method. One should also mention that the treatment of the spin−spin coupling (SSC) in the WFT approach has been developed by Gilka et al.[52] as well as Ganyushin and Neese[53] and implemented in the ORCA program.[54] This code allows one to use either DFT or WFT methods (MRCI, CASSCF, and multireference perturbation theory NEVPT2[55]) to calculate the ZFS[56−66] and has also been successfully applied to several mononuclear inorganic complexes and organic molecules.

Section 2 is devoted to experimental results. Magnetic measurements, single-crystal X-ray diffraction, and HF-HFEPR spectroscopy were performed to experimentally characterize the studied complexes.

Section 3 is devoted to the theoretical description of two of the studied compounds. In the first place, a DFT study leads to the characterization of the main features of the potential energy surfaces. Then, the competition between spin−orbit coupling and Jahn−Teller distortion is studied using first-order spin−orbit calculations. Finally, the ZFS parameters are extracted using more sophisticated calculations accounting for both the first-order and second-order spin−orbit coupling effects.

2. MATERIALS AND METHODS

2.1. Synthesis. Chemicals were purchased from Aldrich and used without further purification. Me_6tren and [Ni(Me_6tren)Br]Br complexes were synthesized according to literature procedures or minor alterations thereof.[67] The synthesis of the [Ni(Me_6tren)(Cl)]-(ClO_4) complex is given in the Supporting Information. All solvents were from BDH and were used as received. All manipulations were conducted under standard laboratory conditions.

2.2. Magnetic Measurement. Variable temperature (300−2 K) magnetic data were measured on powdered samples of **1** and **2** in an eicosane matrix in 1.0 and 0.1 T fields using a Quantum Design MPMS5 superconducting quantum interference device (SQUID) magnetometer. The data were corrected for the diamagnetic contribution of the sample holder and eicosane, and the diamagnetism of the sample was estimated according to Pascal's constants. Low temperature (2−6 K) variable field (0−5.5 T) measurements were carried out in the same manner.

2.3. HF-HFEPR Spectroscopy. Single-crystal HF-HFEPR measurements were carried out in a 31 T resistive magnet using a cavity perturbation technique; in situ sample rotation was possible about a fixed axis.[68] A Millimeter vector network analyzer and several different multipliers were used as a microwave source and detector. Powder spectra were recorded at 5 K on powders pressed into pellets made of either pure ground polycrystalline sample or ground polycrystalline powder dispersed in eicosane. Spectra were recorded with an EPR spectrometer relying on a quasi-optical light transmission. A step-tunable frequency source was used; the final frequency was obtained by multiplying (12 times) a variable synthesizer frequency (10 and 9.58 GHz) or a PDRO source (9.2 GHz). The 220.8 GHz frequency was obtained with the help of a doubler. A Mn(II) reference (MnO diluted in MgO) added to the sample was responsible for the signal at $g = 2$.

2.4. X-ray Diffraction. Single-crystal X-ray diffraction data were measured on a Bruker APEX II CCD diffractometer with graphite−monochromated MoK radiation (λ = 0.71073 Å). Crystals were mounted on a CryoLoop (Hampton Research) with Paratone-N (Hampton Research) as cryoprotectant and then flashfrozen in a nitrogen-gas stream at 100 K. The temperature of the crystal was maintained at the selected value (100 K) by means of a 700 series Cryostream cooling device to within an accuracy of ±1 K. The data were corrected for Lorentz polarization and absorption effects. Diffraction data were also collected at 10 K on a Supernova diffractometer equipped with an ATLAS CCD detector, MoKα radiation and a Helijet open flow cryosystem. The structures at 100 and 10 K were solved by direct methods using SHELXS-97 and refined against F^2 by full-matrix least-squares techniques using SHELXL-97 with anisotropic displacement parameters for all non-hydrogen atoms. Hydrogen atoms were located on a difference Fourier map and introduced into the calculations as a riding model with isotropic thermal parameters. All calculations were performed using the crystal structure crystallographic software package WINGX. See the Supporting Information for further details on the structural analysis.

CCDC 893397 and 912662 contain the supplementary crystallographic data for this paper. These data can be obtained free of charge from the Cambridge Crystallographic Data Centre via www.ccdc.cam.ac.uk/data_request/cif.

2.5. Calculations. DFT calculations were performed using the Gaussian 03 package.[69] The B3LYP functional was used throughout with two different basis sets. The first one is composed of the Hay−Wadt LanL2TZ(f) basis set[70,71] for the nickel metal center, including an f polarization function with an exponent of 3.13, and its corresponding relativistic effective core potential,[71,72] a Pople triple-ζ basis set (6-311G) for N, Cl, and Br atoms,[73] a Pople double-ζ plus polarization basis set (6-31G*) for C atoms,[74] and a Pople double-ζ basis set (4-31G) for H atoms.[75] This basis set (noted basis 1) was used to compute both complexes. The second basis set (basis 2) is much larger and was used to compute compound **1**. It uses a Stuttgart relativistic small-core effective potential for nickel with its associated polarized basis set[76] including two f and one g polarization functions,[77]

a correlation-consistent polarized triple-ζ basis set (cc-pVTZ) for N, and Cl atoms,[78] and a correlation-consistent polarized double-ζ basis set (cc-pVDZ) for C and H atoms.

Although the optimized geometries obtained using both basis sets compare well with the experimental ones, the distances and angles around the Ni(II) ion obtained with basis 1 are closer to the experimental ones. Since the ZFS parameters are very sensitive to the geometrical structure, the geometries of both the minimum and the transition state obtained using basis 1 were selected for the WFT of both compounds.[79]

Unrestricted DFT calculations were used to optimize minima and saddle points of the potential energy surface of the triplet ground state. Spin contamination was negligible, with $\langle S^2 \rangle$ values never exceeding 2.005. Analytical harmonic vibrational frequencies were computed to characterize the nature of the stationary points (all frequencies are positive for the minima and a single imaginary frequency appears for the saddle points) and to evaluate the zero-point vibrational kinetic energy (ZPE).

WFT-based calculations were performed using the MOLCAS 7.4 package.[80] Nondynamic correlation is accounted for by complete active space self consistent field (CASSCF) calculations. The active space is constituted of the 5d orbitals, 5d′ orbitals dedicated to correlation, and the eight d electrons. In order to take into account dynamic correlation effects, CASPT2[81] calculations were performed: (i) CAS(8,10)PT2 calculations for the lowest two triplet states; (ii) CAS(8,10)PT2 calculations for the 10 lowest triplet and 14 lowest singlet states.[82] Spin−orbit couplings are computed within the spin−orbit state interaction frame.[83] This method diagonalizes the spin−orbit matrix between well-chosen CASSCF states. For dynamically correlated calculations, the diagonal elements of the SI matrix are the CASPT2 energies of the computed states. The following ANO-RCC basis sets[84] were used: 6s5p3d1f for Br, 5s4p2d1f for Cl, 6s5p4d2f for Ni, 3s2p1d for N, 3s2p for C, and 2s for H.

3. RESULTS AND DISCUSSION

3.1. Structural Description. The cationic complex $[Ni(Me_6tren)Cl]^+$, previously unreported crystallographically, may be crystallized from a methanolic solution with a perchlorate counterion, giving $[Ni(Me_6tren)Cl](ClO_4)$, (**1**) (Figure 1). The tetrahedral anion, with four potential C_3 axes, readily forms a trigonal crystal system, *R*3*c* in the case of **1**. In accordance with the previously reported structure of $[Ni(Me_6tren)Br]Br$, **2**,[68] compound **1** consists of a Ni(II) ion penta-coordinated by four amino nitrogen atoms from the neutral Me_6tren ligand and one halide ion. The ligands are distributed at the apexes of a trigonal bipyramid with crystallographic C_3 symmetry, the three equatorial sites are occupied by the "terminal" amines, and the axial sites are occupied by the central amine and the chloride ion. The Ni(II) ion lies 0.23 Å below the equatorial plane of the three nitrogen atoms, compared to 0.22 Å in the reported structure of **2**.

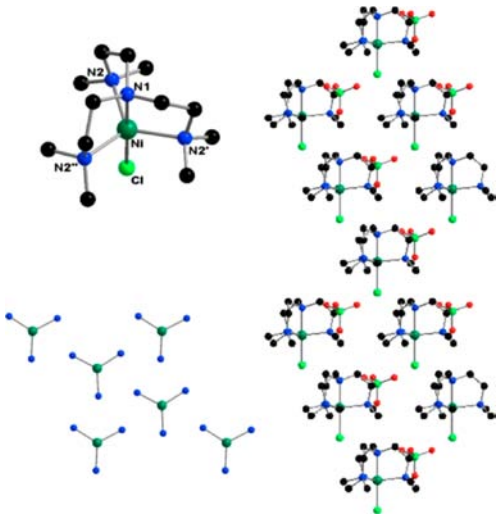

Figure 1. Structure of the cation in $[Ni(Me_6tren)Cl](ClO_4)$ (**1**) (top left) and the same complex viewed along the C_3 axis (bottom left). Packing diagram showing the parallel arrangement of molecular C_3 axes in the solid state (right). Hydrogen atoms are omitted for clarity. Color code: Ni (green), C (black), N (blue), Cl (bright green), O (red).

As highlighted by the selected bond lengths and angles in Table S1 of the Supporting Information, complexes **1** and **2** are structurally similar, and minor differences may be accounted for by greater ionic radius (Ni−X) and the trans effect (Ni−N1) of bromide. There is however a significant difference in the packing of the molecules in the solid state. Complex **2** consists of $[Ni(Me_6tren)Br]^+$ and Br^- ions, crystallized in the cubic $P2_13$ space group. This has a distorted NaCl-type arrangement of ions. As such, when viewing the unit cell along the C_3 axis of any one $[Ni(Me_6tren)Br]^+$ complex, the axes of the three remaining molecules lie pseudoperpendicular, related to one another via threefold rotational symmetry (see the Supporting Information, Figure S1). Replacement of the bromide counterion by the larger and nonspherical perchlorate ion results in the trigonal packing observed for **1** (Figure 1). In this case, the C_3 axes of the molecules all lay parallel and unidirectionally through the unit cell. It may thus be possible to relate molecular magnetic axes to faces and edges of the crystal, facilitating relatively simple interpretation of single-crystal spectroscopic data.

For **1**, upon temperature decrease to 10 K, no space group change associated to a symmetry breaking transition is detected; the molecular crystallographic C_3 symmetry is preserved. The absence of crystal symmetry lowering at 10 K does not rule out the presence of a molecular distortion. Indeed, a local (i.e., molecular) distortion resulting from a Jahn−Teller effect with an equal population of the three distortion modes (see the Supporting Information, Figure S2) and statistically distributed within the single-crystal sample would preserve the *R*3*c* symmetry. The structural dynamics of the $[Ni(Me_6tren)Cl]^+$ complex at 10 K has been examined by performing a TLS (rigid-body thermal motion model) analysis and indicates a possible local (i.e., molecular) structural distortion, whose spatial average maintains the crystal *R*3*c* symmetry (see the Supporting Information, Figure S3).

3.2. Magnetic Measurements. The measured molar magnetic susceptibility (χT) plot for a powdered sample of **1** has a room temperature χT value of 1.42 emu K mol^{-1}, much higher than that expected from the spin-only formula for a high-spin mononuclear Ni(II) complex (1.21 emu K mol^{-1} for g = 2.20), probably due to a large orbital contribution, and is relatively constant down to approximately 120 K. Below this temperature, it collapses, indicating significant ZFS in the S = 1 ground state. Similarly, at 2 K and 5.5 T, the observed magnetization value (1.25 μ_B) is well below the theoretical saturation for an S = 1 system (2.2 μ_B for g = 2.20) and has not reached a plateau. This, along with the fact that the reduced magnetization plots are non-superimposable, is also indicative of large magnetic anisotropy (see the Supporting Information, Figure S4). Very similar results were obtained for **2** (see the Supporting Information, Figure S5). AC susceptibility studies were performed at different frequencies of the oscillating magnetic field, but no out of phase signal was observed down to

dx.doi.org/10.1021/ja308146e | J. Am. Chem. Soc. 2013, 135, 3017−3026

2 K. Hysteresis studies using a microsquid array down to 50 mK did not show any hysteresis at zero field.

3.3. HF-HFEPR Spectroscopy. Given the proposed massive magnetic anisotropy of the complex, and the unreliability of inferring ZFS parameters from magnetic measurements alone, HF-HFEPR measurements were performed on a single crystal of **1**. Careful angle-dependence studies involving rotations of the crystal about a fixed axis were performed to ensure that the applied field was within 2° of the molecular hard plane (see the Supporting Information, Figure S6). Extensive frequency- and temperature-dependence studies (115−250 GHz, 1.4−10 K) were carried out at the field orientation where the EPR transition appears at the highest field, which necessarily corresponds to the field lying in the molecular hard plane (see the Supporting Information, Figure S7). It is notable that the intensities of the observed EPR transitions quickly decrease when the applied field is moved away from the molecular hard plane, which indicates that the transition matrix element vanishes when the applied field is out of the molecular hard plane. Two EPR transitions (**A** and **B**) were observed (see the Supporting Information, Figure S8) at frequencies between 115 and 240 GHz (see the Supporting Information, Figures S9 and S10). EPR experiments were repeated on several different crystals, and similar spectra were observed. For an S = 1 system, only one ground-state transition is expected; however, both of these signals were confirmed to be ground-state transitions through temperature-dependence studies (see the Supporting Information, Figure S8). We propose that the crystallographically observed molecular C_3 symmetry is broken by a Jahn−Teller-type distortion that is within the molecular triangular planes. By assuming that the easy axes of all molecules remain parallel and that the space group of the crystal remains unchanged, this yields three different molecular orientations (**A**, **B**, and **C**) that are related by a threefold rotational symmetry (see the Supporting Information, Figure S11). The molecules have equal probability ($^1/_3$) of falling in any one of these orientations. Thus, the hard axes (x axes) of the molecules are not parallel to one another giving rise to the multiple transitions that were observed experimentally. This distortion also permits the observation of a rhombic E term that is strictly forbidden if rigorous molecular C_3 symmetry is maintained. We note that the hard planes corresponding to the **A** and **B** molecules vary slightly by a few degrees (see the Supporting Information, Figure S6 inset), implying that the easy axes of the **A** and **B** molecules are not exactly parallel. Such an observation further supports our assumption that the local molecular symmetry is lowered by Jahn−Teller-type distortions at low temperatures; that is, with the presence of distortions, the anisotropy tensors of the molecules are tilted; thus, the easy axes of molecules do not coincide with the crystallographic threefold screw axes. However, the space group of **1** remains unchanged; hence, these three molecular species are related by a threefold rotation. Variable-frequency studies were performed with the field applied in the hard planes of the **A** and **B** molecules, respectively, to study the frequency dependence of these transitions (see the Supporting Information, Figures S9 and S10).

The EPR data were simulated employing the following Hamiltonian, where φ represents the angle between the field and the molecular hard axes (Figure 2):

$$\hat{H} = D\hat{S}_z^{\,2} + E(\hat{S}_x^{\,2} - \hat{S}_y^{\,2}) + \mu_B \cdot g \cdot B(\cos(\varphi)\hat{S}_x + \sin(\varphi)\hat{S}_y) \quad (1)$$

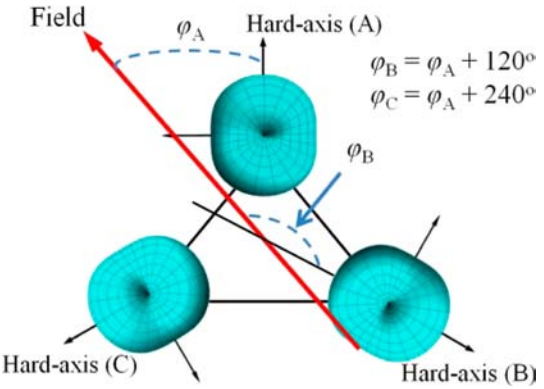

Figure 2. Origin of φ in the Hamiltonian used to fit the EPR data. The "donuts" represent the zero-field anisotropy surface of the molecules assuming the previously described Jahn−Teller distortion.

The value of g was fixed at 2.4 (extracted from the room temperature χT value) and the values of D, E, and φ were varied across a large parameter space. Due to the fact that we were only able to perform single-axis rotation, the field orientation in the molecular hard plane (φ) remains an arbitrary experimental parameter. Simulations gave the following best fit parameters: D = −179 cm^{-1}, E = 1.63 cm^{-1}, φ_A = 105.5°, and φ_B = 225.5°, as shown in Figure 3.

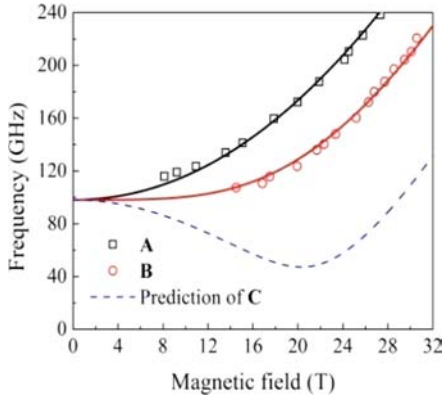

Figure 3. EPR peak positions observed for the **A** and **B** molecular transitions of a single crystal of **1**, with the field aligned in the magnetic hard plane of the **A** (black squares) and **B** (red circles) molecules, respectively. The solid lines correspond to the best fit employing the Hamiltonian (eq 1) and parameters given in the text. The dashed blue line represents the predicted positions of the EPR transitions associated with the **C** molecules.

The solid lines represent the simulations of the EPR peak positions associated with the **A** and **B** molecules. It should be noted that, for this parameter set, the predicted transitions for the **C** molecules will appear at lower frequency (Figure 3, dashed blue line) and thus were not observed experimentally. To test uncertainties associated with these parameters, each two parameters were fixed in turn, and the error associated with the simulation was calculated while the others were varied (see the Supporting Information, Figures S12−S17). These tests show a near linear dependence on D and g (see the Supporting Information, Figure S15). This is of little surprise given that it is impossible to directly measure the large ZFS of **1** (~200 cm^{-1}) by EPR. The value of D was obtained indirectly by fitting the observed hard plane transitions (see the Supporting Informa-

dx.doi.org/10.1021/ja308146e | J. Am. Chem. Soc. 2013, 135, 3017−3026

tion, Figure S5), and g has the effect of scaling the Zeeman energy used to calculate the zero-field parameters. Since the field is always applied in the hard plane, the g value in the analysis corresponds to the perpendicular g value, $g_{x,y}$. It is likely that g_z is not equal to $g_{x,y}$, which should be taken into account in subsequent analysis.

The experiment does however show unambiguous evidence of the presence of a sizable E term, whose magnitude (1.6 cm^{-1}) is clearly independent of g, D, and φ (see the Supporting Information, Figures S12, S13, S16, and S17). The presence of rhombic anisotropy provides spectroscopic proof that the molecular C_3 symmetry is broken by Jahn−Teller-type distortions. In summary, the EPR measurements of **1** provide a clear determination of the magnitude of the transverse anisotropy and demonstrate the dependence of D on the g value. Even for a g value of 2.0, which would be very low given the near first-order spin−orbit coupling predicted for **1**, D is expected to be as large as -120 cm^{-1}, with a value approaching -180 cm^{-1}, more likely.

In order to check the analysis of the high-field EPR measurements performed on a single crystal, powder spectra were also recorded (on powders pressed into pellets). Indeed, with a $|D|$ value higher than 100 cm^{-1}, one cannot expect to observe the corresponding transitions even using high frequencies. Conversely, transitions associated with the E term can be observed on powder spectra at low field, that is, for frequencies only slightly larger than the energy gap. In Figure S18 (see the Supporting Information), spectra recorded at 5 K and at four different frequencies, ranging from 110 to 221 GHz, are displayed. The shift of the main line with frequency leads to the following parameters: $E = 1.56 \pm 0.05$ cm^{-1} and $g_z = 2.34 \pm 0.07$. Even if these figures are not very precise due to the limited frequency (and field) interval where they are observed, as this transition becomes weaker and weaker with the increase of the Zeeman interaction, the E and g_z values are close to the ones obtained from single-crystal measurements, thus supporting the analysis previously developed on the single crystal. It may be noticed that, for the powder measurements, more than one signal is observed except at the lowest frequency. This seems to point towards the existence of molecules with different anisotropies, which could contribute to the extra signals observed on the single-crystal spectra (especially the one appearing only slightly lower in field than the **A** signal).

Similar measurements were performed on **2**; however, multiple peaks were observed, and even the most prominent feature could be modeled with a range of parameters. The poor quality of the data reflects the difficulties associated with single-crystal measurements for **2**, where the nonparallel alignment of the molecular easy axes within the unit cell prevents the simultaneous application of the field in all of the molecular hard planes. This greatly complicates the spectra, preventing any meaningful analysis of the ZFS parameters. Future investigation may require the replacement of the bromide counterion with perchlorate, in an attempt to change the crystal system and to obtain results comparable to those for **1**. Despite the experimental difficulties associated with **2**, the ZFS parameters obtained for **1** represent a near 10-fold increase in axial anisotropy for a reported Ni(II) complex.

3.4. Theoretical Investigation. *3.4.1. Potential Energy Surface Features: a DFT Study.* Experimentally, the observed symmetry of the complexes under study is C_3. The spin multiplicity of the electronic ground state is triplet. Because of the spatial degeneracy, the ground state corresponds to a doubly degenerate ^3E state at this peculiar geometry. Due to Jahn−Teller effects, one expects the degeneracy of this state to be lifted following appropriate symmetry-breaking distortions. This gives rise to a moat surrounding a Jahn−Teller C_3 conical intersection, with three symmetry-equivalent minima and saddle points (transition states TS),[85] as shown in Figure 4.

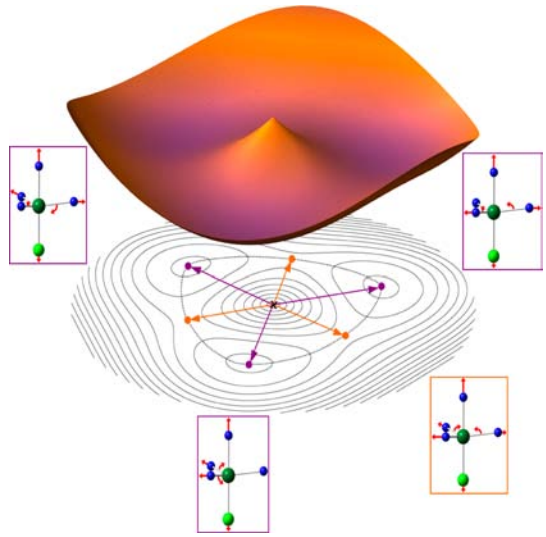

Figure 4. Schematic representation of a moat around a Jahn−Teller C_3 crossing showing the three symmetry-equivalent minima and TSs: three-dimensional representation (the tricorn, top) and equipotential contour plot (bottom). The main displacement vectors pointing to the minima (purple boxes) and to one transition state (red box) are shown.

Unrestricted DFT calculations were used to optimize these minima and saddle points allowing one to evaluate the pseudorotation barrier around the moat. Gatteschi and co-workers have already invoked a dynamic Jahn−Teller effect for these types of complexes.[86]

The degenerate ground state ^3E in the C_3 symmetry point group (SPG) is split in the C_1 SPG upon the Jahn−Teller effect in two states that differ by their electronic configuration, either $d_{xz}^2 d_{yz}^2 d_{x^2-y^2}^2 d_{xy} d_{z^2}$ or $d_{xz}^2 d_{yz}^2 d_{xy}^2 d_{x^2-y^2} d_{z^2}$ (see Figure 5), for

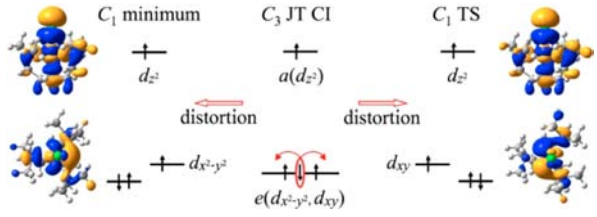

Figure 5. Electronic configuration and singly occupied molecular orbitals of the C_1 minimum state (left, $|d_{x^2-y^2}|$) and TS (right, $|d_{xy}|$). The main displacement vectors of both distortions are given in Figure 4.

which the associated determinants will be noted $|d_{xy}|$ and $|d_{x^2-y^2}|$ hereafter. One of them corresponds to a true minimum of the potential energy surface while the other one corresponds to the TS (saddle point) connecting two minima.

The main geometrical parameters of the optimized C_1 minimum, the TS, and the experimental C_3 structures are given in Table S2 of the Supporting Information for comparison. Figure S19 of the Supporting Information gives

dx.doi.org/10.1021/ja308146e | J. Am. Chem. Soc. 2013, 135, 3017−3026

the numbering of the atoms used in the table. In order to appreciate the magnitude of the distortion, we use the parameters δr and $\delta\alpha$ that quantify independently the distance distortion and the angular distortion (see the Supporting Information, eq S1).

The values of δr and $\delta\alpha$ are also reported in Table S2 (see the Supporting Information) showing that (i) for both compounds the angular deformation is more pronounced than the distance deformation and (ii) the Jahn−Teller distortion is almost identical for both compounds.

From the vibrational contributions, the ZPEs have been computed for the geometry of both the minima and the TSs. For compound **1**, the electronic energy barrier is 83.6 cm^{-1}. By adding the ZPE contributions to both the C_1 minimum ground state and the TS energies, the energy barrier is reduced to 75.1 cm^{-1} (108 K). For compound **2**, the energy barrier including the ZPE is 35 cm^{-1} (50 K). These very weak values rationalize the fact that the X-ray structures of both compounds determined at 100 K were found symmetric, that is, of the C_3 SPG.

3.4.2. Competition between the Antagonist Effects of the First-Order Spin−Orbit Coupling and the Jahn−Teller Distortion: a Two-State Spin−Orbit CAS(8,10)PT2 Study. In order to quantify the antagonist effects of the first-order spin−orbit coupling and the Jahn−Teller distortion, the energy of the spin−orbit states arising from the degenerate ground term (in C_3 SPG) have been calculated using the SOSI method for different geometries interpolated between the experimental geometry and the DFT minimum. Since at this stage we just want to describe the first-order effects of the SOC, only the two spin−orbit free states arising from the two spatial configurations were introduced in the SOSI matrix. Their wave functions have been optimized using minimal active space CAS(8,10)SCF calculations while their energies, used in the SOSI calculations, are the dynamically correlated CAS(8,10)-PT2 ones. The spectrum computed for **1** as a function of the distortion between the C_3 and the DFT minimum geometry is given in Figure 6.

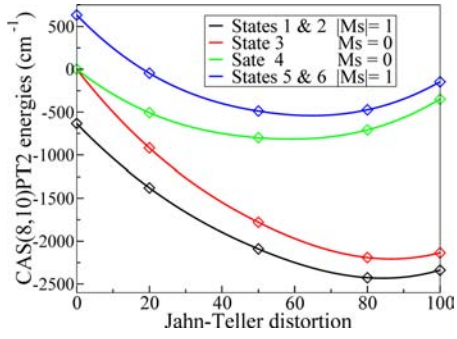

Figure 6. Low-energy spectrum of **1** computed at the two-state SOSI-CAS(8,10)PT2 level of correlation. The x axis represents a linear distortion between the C_3 (0) and the DFT C_1 minimum (100).

The geometries along the distortion are obtained by a linear interpolation between the two extreme structures. The spatial configuration in which d_{xy} is singly occupied is stabilized while the $d_{x^2-y^2}$ one is destabilized. While the $M_s = \pm 1$ components are degenerate whatever the distortion is, the $M_s = 0$ components are split by the distortion. One may notice that the SOSI-CAS(8,10)PT2 constrained minimum (along this distortion) is located at 50% between the C_3 and the C_1 DFT geometries. The geometry at this minimal energy is less distorted than the DFT one, and the energy difference between the $M_s = \pm 1$ components and the $M_s = 0$ one is therefore larger at the SOSI-CASPT2 constrained minimum than at the DFT minimum. One should mention that the SOSI-CASSCF constrained minimum is located at 75% of the C_1 structure. The spectrum of compound **2** is represented in Figure S20 of the Supporting Information. It exhibits the same features except that the SOSI-CASSCF and SOSI-CASPT2 constrained minima are both located at 80% between the C_3 and DFT C_1 geometries.

In the C_3 SPG (zero of the abscissa), the degeneracy between the $d_{x^2-y^2}$ and d_{xy} orbitals is responsible for the very important effect of the spin−orbit interaction: the spin−orbit operator directly couples the M_s components of the two spatial configurations, that is, spin−orbit interaction acts at first order. Indeed, the $d_{x^2-y^2}$ and d_{xy} orbitals are linear combinations of the complex d_{2-} and d_{2+} orbitals. The operator $\sum_i \zeta_i \hat{l}_{Zi} \cdot \hat{s}_{Zi}$ therefore couples the degenerate spatial components of the ^3E ground term, which differ by the occupation of the $d_{x^2-y^2}$ and d_{xy} orbitals. Actually only the $M_s = -1$ and $M_s = +1$ of the two spatial configurations are coupled resulting in a removal of degeneracy of the three M_s components. The usual ZFS Hamiltonian cannot model the spectrum, at this C_3 symmetry, since the ground term presents a first-order angular momentum. The values of the angular momentum components are very close to $M_l = \pm 2$. For this peculiar geometry, the spin−orbit momentum components M_J can be defined from the values of M_l and M_s. Their values are $M_J = 3, 2, 1, -1, -2$, and -3. The energy splitting between the $M_s = \pm 1$ and the $M_s = 0$ states of the ground term is around 635 cm^{-1} for both compounds, which is a value very close to the spin−orbit coupling constant of the Ni(II) ion, 644 cm^{-1}.[87]

The Jahn−Teller distortion induces a lifting of degeneracy of the $d_{x^2-y^2}$ and d_{xy} orbitals, which results in a lifting of degeneracy of the spatial configurations by the quantity $\pm \delta_1$ and therefore a reduction of the splitting due to the spin−orbit coupling. As soon as the symmetry is lowered by the distortion, the two configurations $|d_{xy}|$ and $|d_{x^2-y^2}|$ are coupled by the ligand field, by the quantity δ_2. The here-proposed model is similar to that used in similar contexts.[24,88] The representative matrix of the model Hamiltonian involving the spin−orbit coupling between the two configurations $|d_{xy}|$ and $|d_{x^2-y^2}|$ and the Jahn−Teller distortion ligand field parameters (δ_1 and δ_2) is given below (eq 2):

$$
\begin{array}{c}
 \\
\langle d_{xy},-1| \\
\langle d_{x^2-y^2},-1| \\
\langle d_{xy},0| \\
\langle d_{x^2-y^2},0| \\
\langle d_{xy},1| \\
\langle d_{x^2-y^2},1|
\end{array}
\begin{array}{c}
\begin{array}{cccccc}
|d_{xy},-1\rangle & |d_{x^2-y^2},-1\rangle & |d_{xy},0\rangle & |d_{x^2-y^2},0\rangle & |d_{xy},1\rangle & |d_{x^2-y^2},1\rangle
\end{array} \\
\begin{pmatrix}
-\Delta+\delta_1 & \delta_2+i\zeta & 0 & 0 & 0 & 0 \\
\delta_2-i\zeta & -\Delta-\delta_1 & 0 & 0 & 0 & 0 \\
0 & 0 & -\Delta+\delta_1 & \delta_2 & 0 & 0 \\
0 & 0 & \delta_2 & -\Delta-\delta_1 & 0 & 0 \\
0 & 0 & 0 & 0 & -\Delta+\delta_1 & \delta_2-i\zeta \\
0 & 0 & 0 & 0 & \delta_2+i\zeta & -\Delta-\delta_1
\end{pmatrix}
\end{array}
\tag{2}
$$

where ζ is the spin−orbit constant of Ni(II) reduced by the ligand field and Δ is the mean value of the eigenenergies. The values of δ_1, δ_2, and Δ depend on the geometrical structure. For the C_3 SPG, the three parameters are zero while they are maximal for the most distorted geometry of the DFT C_1 minimum. The diagonalization of this matrix gives access to

dx.doi.org/10.1021/ja308146e | J. Am. Chem. Soc. 2013, 135, 3017−3026

the energy of the six spin−orbit states. The general expressions of the energies are

$$E_{1,2}(M_s = \pm 1) = -\Delta - \sqrt{\delta^2 + \zeta^2}$$
$$E_{3,4}(M_s = 0) = -\Delta \pm \delta$$
$$E_{5,6}(M_s = \pm 1) = -\Delta + \sqrt{\delta^2 + \zeta^2} \quad (3)$$

where (1,2), (3,4) and (5,6) are ordered by increasing energy and $\delta^2 = {\delta_1}^2 + {\delta_2}^2$. In the C_3 geometry ($\delta = 0$, $\Delta = 0$), these energies are:

$$E_{1,2}(M_J = \pm 3) = -\zeta$$
$$E_{3,4}(M_J = \pm 2) = 0$$
$$E_{5,6}(M_J = \pm 1) = \zeta \quad (4)$$

When the distortion is dominant ($\delta^2 \gg \zeta^2$), the eigenstates are very similar to the spin−orbit free states and their energies are

$$E(^3A)_1 = -\Delta - \delta$$
$$E(^3A)_2 = -\Delta + \delta \quad (5)$$

While only values of δ and Δ are accessible from the computed energies, it is possible to determine the values of Δ, δ, δ_1, and δ_2 using both the energies and wave functions from the effective Hamiltonian theory in the formalism of des Cloizeaux.[89] This theory enables one to build a numerical effective Hamiltonian working in the model space constituted of the components of the two spatial configurations and fulfilling the following conditions:

$$H^{eff}|\tilde{\Psi}_i\rangle = E_i|\tilde{\Psi}_i\rangle \quad (6)$$

where E_i are the ab initio energies of the lowest spin−orbit states and $|\Psi\rangle$ are the orthonormalized projections onto the model space of the corresponding spin−orbit states. According to this theory, the numerical elements of the effective Hamiltonian matrix can be calculated from the spin−orbit energies and wave functions, using the spectral decomposition of the effective Hamiltonian:

$$\langle I|\hat{H}^{eff}|J\rangle = \langle I|\sum_i E_i|\tilde{\Psi}_i\rangle\langle\tilde{\Psi}_i|J\rangle \quad (7)$$

where I and J are the M_s components of the two spatial configurations, that is, the functions on which is spanned the analytical matrix (eq 2). Identifying the analytical elements and the numerical ones enables one to extract the values of all the interactions of the model. Table S3 of the Supporting Information reports the values of δ, δ_1, δ_2, Δ, and ζ (in cm^{-1}) determined for the experimental geometry, the DFT minimum, and the SOSI-CASSCF and the SOSI-CASPT2 constrained minima.

The changes of metal−ligand covalency between the different studied geometries have a negligible impact on the ζ value, since calculations show that this parameter is essentially constant. It is worth noticing that this value is far from being negligible in comparison to the value of δ, showing that (i) eq 3 should be used to reproduce the computed energies and (ii) the impact on the spectrum of the spin−orbit coupling is still very important even at the most distorted geometry (DFT minimum) justifying the terminology "first order". Of course, all the values of the introduced ligand field parameters are zero at the C_3 geometry. As expected the values of δ, δ_1 (stabilization/destabilization of the configurations), and δ_2 (mixing of the two configurations) increase with the deformation. One may also notice that the signs of δ_1 and δ_2 change between the minima and the TS, reflecting the interchange of the dominant configuration in the ground-state wave function. Finally, one may notice that Δ is positive at the SOSI-CASPT2 minimum (and for more distorted geometries) reflecting the fact that, for compound **1**, the stabilization of the ground state due to the Jahn−Teller distortion is very weak: since the excited states are destabilized by the distortion, the mean energy value is consequently positive.

3.4.3. Determination of the ZFS Parameters: a 24 State SOSI-CAS(8,10)PT2 Study. When the geometry is distorted, the impact on the spectrum of the spin−orbit coupling between the two first states decreases, and the spin−orbit effects resulting from the coupling with the other excited states may become of comparable importance. In order to better describe the lowest energy spectrum and in particular the lifting of degeneracy of the M_s components of the ground term, SOSI-CAS(8,10)PT2 calculations involving the 10 excited triplets and 14 excited singlets have been performed. The low energy spectrum reported in Figure S21 of the Supporting Information exhibits the same qualitative features as the one obtained from the two-state SOSI matrix. The main qualitative differences are (i) a slight reduction of the ζ spin−orbit coupling constant (595 versus 630 cm^{-1}) and (ii) the lifting of degeneracy of the $M_s = \pm 1$ components that results from the spin−orbit coupling with the other excited terms. For distorted structures, the energies of the three spin−orbit states arising from the ground term configuration can be described using the ZFS Hamiltonian $\hat{H}^{ZFS} = \hat{S}.\overline{\overline{D}}.\hat{S}$ given by eq 1 in zero field $\mathbf{B} = 0$. Using the effective Hamiltonian theory, it is possible to extract all the components of the 2nd rank ZFS tensor $\overline{\overline{D}}$. Then, its diagonalization gives access to the axial and rhombic D and E parameters and to the magnetic axes frame. The so-obtained axes of compounds **1** and **2** are represented in Figure S22 of the Supporting Information, showing that the Z axis determined theoretically is very close to the Ni−X direction.

Table 1 reports the extracted values of the D and E parameters for the four different computed geometrical structures: the C_1 DFT minimum, the constrained SOSI-CASSCF and SOSI-CASPT2 minima, and the TS geometry. It is worth noticing that, while the reduction of the values of D when introducing the spin−orbit coupling between the ground electronic term and the excited ones is non-negligible, the values are still extremely large, ranging between −100 and −200 cm^{-1}.

As shown previously,[48] the methods used here usually provide reliable values of the ZFS parameters for the experimental geometries. Since, the property is governed by both the spin−orbit coupling and the symmetry lowering (from isotropic symmetry) of the geometry, the results strongly depend on the geometrical structure. Unfortunately, the distorted experimental geometries of these compounds are not available.

In order to appreciate which of these geometries is the most reliable, we have computed both magnetization versus magnetic field $M = f(B/T)$ and susceptibility versus temperature $\chi T = f(T)$. Figures 7 and S23 (Supporting Information) show the results obtained for the SOSI-CASSCF minimum for which the

Table 1. ZFS Parameters (cm^{-1}) Computed at Several Levels of Calculations for the Geometries of the TS, the DFT Minimum, and the SOSI-CASSCF and SOSI-CAS(8,10)PT2 Constrained Minima (along the Jahn−Teller Distortion between the Experimental C_3 and the DFT Minimum)[a]

		1		2	
level of calculation	geometry	*D*	*E*	*D*	*E*
CAS(8,10)PT2 2 triplets	DFT minimum	−187	0	−202	0
	SOSI-CASSCF constrained minimum	−241	0	−234	0
	SOSI-CASPT2 constrained minimum	−299	0	−234	0
	TS minimum	−224	0	−240	0
CAS(8,10)PT2 14 singlets and 10 triplets	DFT minimum	−104	0.7	−117	1.1
	SOSI-CASSCF constrained minimum	−152	0.6	−147	1.1
	SOSI-CASPT2 constrained minimum	−205	0.8	−147	1.2
	TS minimum	−127	3.0	−146	3.1

[a]The number of states, which have been introduced in the state interaction matrix, is indicated in the left column.

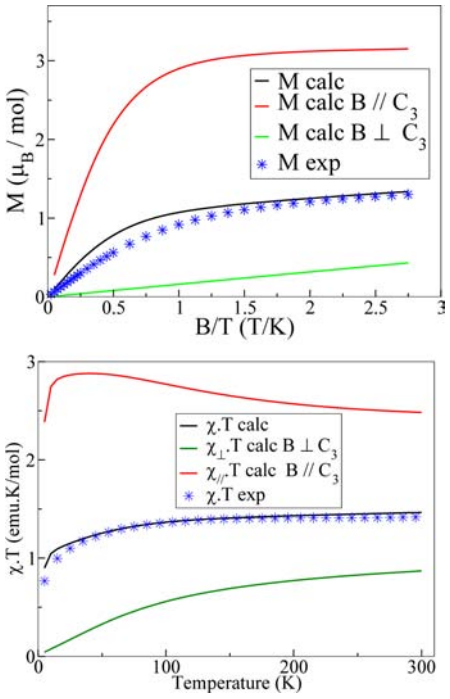

Figure 7. $M = f(B/T)$ at 2 K and $\chi T = f(T)$ curves computed from the 24 state SOSI-CASPT2 solutions at the constrained SOSI-CASSCF minimum for **1**. The experimental results are reported for comparison.

best agreement with the experiment is obtained for both $M = f(B/T)$ and $\chi T = f(T)$ (see the Supporting Information, Figures S24 and S25, for comparison with the other geometries). At the SOSI-CASSCF minimum, the value of D is -152 cm^{-1}, which is in agreement with the best estimate -180 cm^{-1} from HF-HFEPR measurements.

Looking more carefully at the SOSI matrix, one may notice that the main contributions to the ZFS are brought by the three first excited triplet states. The first excited triplet (dominated by the $|d_{x^2-y^2}|$ configuration) brings the large negative contribution. The coupling with the other excited states and in particular with the third and fourth triplet states resulting from excitations from the d_{xz} and d_{yz} orbitals to the d_{z^2}, d_{xy}, and $d_{x^2-y^2}$ orbitals bring positive contributions that again reduce the D value. Comparing all the obtained values, one may conclude that the Jahn−Teller distortion is mainly responsible for the reduction of the D values. Indeed the lifting of degeneracy between the two spatial components of the ground term induces a reduction of the energy difference between the $M_s = \pm 1$ and $M_s = 0$ lowest components from -595 cm^{-1} (in the C_3 structure) to -241 cm^{-1} for instance at the constrained SOSI-CASSCF minimum while the total positive contribution brought by the other excited states is 85 cm^{-1}.

In summary, while the reduction of D due to the Jahn−Teller distortion is quite important, the values of D in all considered distorted structures are still extremely large in comparison to what is usually observed in mononuclear complexes. This result shows that, in the studied complexes, the Jahn−Teller distortion is not large enough to completely eliminate the large impact of the spin−orbit coupling between the two lowest states. The rigidity of the ligand preventing strong deformations is probably responsible for this result.

It was unfortunately not possible to characterize compound **2** using HF-HFEPR spectroscopy. Nevertheless, both magnetic measurements and theoretical investigations show that this compound also exhibits a giant uniaxial magnetic anisotropy with a $D = -147$ cm^{-1} value close to that of compound **1**. This result is in line with the fact that the geometrical distortion mainly due to angular contributions is similar in both compounds.

4. CONCLUDING REMARKS

Ni(II) complexes with a trigonal bipyramid symmetry, as is the case for **1** and **2**, must have a doubly degenerate ground state and thus a first-order spin−orbit coupling leading to a magnetic anisotropy of the order of the spin−orbit parameter (around 600 cm^{-1}). It is expected that, in order to gain energy, vibronic coupling lifts the degeneracy of the ground state thus drastically reducing the effect of first-order spin−orbit coupling and consequently magnetic anisotropy. In such cases, the energy difference between the M_s components of the S = 1 state is drastically reduced. In order to estimate the magnitude of the magnetic anisotropy in compound **1** that has a C_3 crystallographic axis, EPR studies were performed on a single crystal and on powder samples. These studies allowed showing that the M_s sublevels ±1 are the lowest in energy. The rhombic ZFS parameter E was determined (1.6 cm^{-1}), and the axial parameter D was estimated to be larger than 120 cm^{-1}, showing that the orbital momentum is not fully quenched. In order to rationalize the magnetic behavior and to get insight into the origin of the large Ising-type magnetic anisotropy experimentally observed, a full theoretical study was carried out. DFT calculations show that, due to Jahn−Teller effects, the potential energy surfaces of the studied complexes exhibit a moat around a conical intersection. The potential energy barrier including vibrational contributions is relatively flat.

The theoretical studies, the EPR results, and the structural analysis at 10 K of complex **1** lead to the important conclusion that the Jahn−Teller effect only weakly distorts the structure. As a consequence, a giant axial anisotropic parameter is found, resulting from a non-totally quenched orbital angular momentum. The origin of such a weak Jahn−Teller effect can be attributed to the rigidity of the Me_6tren pentadentate

dx.doi.org/10.1021/ja308146e | J. Am. Chem. Soc. 2013, 135, 3017−3026

ligand imposing a robust trigonal bipyramidal geometry that counterbalances the Jahn−Teller distortion. This highlights the crucial role played by the organic ligands in designing mononuclear complexes with large magnetic anisotropy. Such complexes can be used as building-block units for the elaboration of polynuclear complexes with high blocking temperatures.

■ ASSOCIATED CONTENT

Supporting Information

Crystallographic data as CIF files; structural data and their analysis at 100 K for **1** and **2** and at 10 K for **1**; SQUID magnetic data on powder; angular dependence and analysis of the EPR spectra of a single crystal of **1**; powder EPR spectra of **1** at frequencies between 110 and 221 GHz; theoretical variation of the energy levels for **1** and **2** upon the magnitude of the Jahn−Teller distortion; and calculated magnetic data. This material is available free of charge via the Internet at http://pubs.acs.org.

■ AUTHOR INFORMATION

Corresponding Author

*nathalie.guihery@irsamc.ups-tlse.fr; shill@magnet.fsu.edu; talal.mallah@u-psud.fr

Notes

The authors declare no competing financial interest.

■ ACKNOWLEDGMENTS

We thank the CNRS (Centre National de la Recherche Scientifique), the Université Paris Sud 11, the Université Paul Sabatier-Toulouse III, and the Agence Nationale de la Recherche ANR (project TEMAMA ANR-09-BLAN-0195-01) for financial support. Work performed at the National High Magnetic Field Laboratory was supported by the NSF (grant nos. DMR0654118 and CHE0924374) and the State of Florida.

■ REFERENCES

(1) Sessoli, R.; Tsai, H. L.; Schake, A. R.; Wang, S. Y.; Vincent, J. B.; Folting, K.; Gatteschi, D.; Christou, G.; Hendrickson, D. N. *J. Am. Chem. Soc.* **1993**, *115*, 1804.

(2) Sessoli, R.; Gatteschi, D.; Caneschi, A.; Novak, M. A. *Nature* **1993**, *365*, 141.

(3) Gatteschi, D.; Sessoli, R.; Villain, J. *Molecular Nanomagnets*; Oxford University Press: New York, 2006; and references therein.

(4) Milios, C. J.; Vinslava, A.; Wernsdorfer, W.; Moggach, S.; Parsons, S.; Perlepes, S. P.; Christou, G.; Brechin, E. K. *J. Am. Chem. Soc.* **2007**, *129*, 2754.

(5) Yoshihara, D.; Karasawa, S.; et Koga, N. *J. Am. Chem. Soc.* **2008**, *130*, 10460.

(6) Mannini, M.; Pineider, F.; Sainctavit, P.; Danieli, C.; Otero, E.; Sciancalepore, C. A.; Talarico, M.; Arrio, M.-A.; Cornia, A.; Gatteschi, D.; Sessoli, R. *Nat. Mater.* **2009**, *8*, 194.

(7) Leuenberger, M. N.; Loss, D. *Nature* **2001**, *410*, 789.

(8) Ardavan, A.; Rival, O.; Morton, J. J. L.; Blundell, S. J.; Tyryshkin, A. M.; Timco, G. A.; Winpenny, R. E. P. *Phys. Rev. Lett.* **2007**, *98*, 057201.

(9) Stamp, P. C. E.; Gaita-Arino, A. *J. Mater. Chem.* **2009**, *19*, 1718.

(10) Ishikawa, N.; Sugita, M.; Ishikawa, T.; Koshihara, S.-Y.; Kaizu, Y. *J. Am. Chem. Soc.* **2003**, *125*, 8694.

(11) Ishikawa, N.; Sugita, M.; Ishikawa, T.; Koshihara, S.; Kaizu, Y. *J. Phys. Chem. B* **2004**, *108*, 11265.

(12) AlDamen, M. A.; Clemente-Juan, J. M.; Coronado, E.; Marti-Gastaldo, C.; Gaita-Arino, A. *J. Am. Chem. Soc.* **2008**, *130*, 8874.

(13) AlDamen, M. A.; Cardona-Serra, S.; Clemente-Juan, J. M.; Coronado, E.; Gaita-Arino, A.; Marti-Gastaldo, C.; Luis, F.; Montero, O. *Inorg. Chem.* **2009**, *48*, 3467.

(14) Rinehart, J. D.; Long, J. R. *J. Am. Chem. Soc.* **2009**, *131*, 12558.

(15) Harman, W. H.; Harris, T. D.; Freedman, D. E.; Fong, H.; Chang, A.; Rinehart, J. D.; Ozarowski, A.; Sougrati, M. T.; Grandjean, F.; Long, G. J.; Long, J. R.; Chang, C. J. *J. Am. Chem. Soc.* **2010**, *132*, 1224.

(16) Rogez, G.; Rebilly, J. N.; Barra, A. L.; Sorace, L.; Blondin, G.; Kirchner, N.; Duran, M.; van Slageren, J.; Parsons, S.; Ricard, L.; Marvilliers, A.; Mallah, T. *Angew. Chem., Int. Ed.* **2005**, *44*, 1876. Krzystek, J.; Park, J.-H.; Meisel, M. W.; Hitchman, M. A.; Stratemeier, H.; Brunel, L.-C.; Telser, J. *Inorg. Chem.* **2002**, *41*, 4478. Vongtragool, S.; Gorshunov, B.; Dressel, M.; Krzystek, J.; Eichhorn, D. M.; Telser, J. *Inorg. Chem.* **2003**, *42*, 1788.

(17) Edelstein, N. M.; et Lander, G. H. *The Chemistry of the Actinide and Transactinide Elements*, 3rd ed.; Morss, L. R., Edelstein, N. M., Fuger,J., Katz, J. J., Eds.; Springer: Dordrecht, The Netherlands, 2006; Vol. *4*.

(18) Orchard, A. F. *Magnetochemistry*; Oxford University Press: Oxford, U.K., 2003.

(19) Rinehart, J. D.; Harris, T. D.; Kozimor, S. A.; Bartlett, B. M.; Long, J. R. *Inorg. Chem.* **2009**, *48*, 3382.

(20) Benelli, C.; Gatteschi, D. *Chem. Rev.* **2002**, *102*, 2369.

(21) Laplaza, C. E.; Cummins, C. C. *Science.* **1995**, *268*, 861.

(22) Atanasov, M.; Comba, P.; Daul, C. A. *Inorg. Chem.* **2008**, *47*, 2449.

(23) Atanasov, M.; Busche, C.; Comba, P.; El Hallak, F.; Martin, B.; Rajaraman, G.; van Slageren, J.; Wadepohl, H. *Inorg. Chem.* **2008**, *47*, 8112.

(24) Atanasov, M.; Ganyushin, D.; Pantazis, D. A.; Sivalingam, K.; Neese, F. *Inorg. Chem.* **2011**, *50*, 7460.

(25) Jahn, H. A.; Teller, E. *Proc. R. Soc. London, Ser. A* **1937**, *161*, 220.

(26) Bersuker, I. B. *The Jahn-Teller Effect and Vibronic Interactions in Modern Chemistry*; Plenum Press: New York, 1984.

(27) Bersuker, I. B. *The Jahn-Teller Effect*; Cambridge University Press: Cambridge, U.K., 2006.

(28) Bersuker, I. B.; Polinger, V. Z. *Vibronic Interactions in Molecules and Crystals*; Springer: Berlin, Germany, 1989.

(29) Webb, S. P.; Gordon, M. S. *J. Chem. Phys.* **1998**, *109*, 919.

(30) Pederson, M. R.; Jackson, K. A. *Phys. Rev. B* **1990**, *41*, 7453.

(31) Jackson, K. A.; Pederson, M. R. *Phys. Rev. B* **1990**, *42*, 3276.

(32) Pederson, M. R.; Khanna, S. N. *Phys. Rev. B* **1999**, *60*, 9566.

(33) Baruah, T.; Pederson, M. R. *Int. J. Quantum Chem.* **2003**, *93*, 324.

(34) Kortus, J.; Pederson, M. R.; Baruah, T.; Bernstein, N.; Hellberg, C. S. *Polyhedron* **2003**, *22*, 1871.

(35) Park, K.; Pederson, M. R.; Richardson, S. L.; Aliaga-Alcalde, N.; Christou, G. *Phys. Rev. B* **2003**, *68*, 020405.

(36) Ribas-Ariño, J.; Baruah, T.; Pederson, M. R. *J. Chem. Phys.* **2005**, *123*, 044303.

(37) Ribas-Ariño, J.; Baruah, T.; Pederson, M. R. *J. Am. Chem. Soc.* **2006**, *128*, 9497.

(38) Ruiz, E.; Cirera, J.; Cano, J.; Alvarez, S.; Loose, C.; Kortus, J. *Chem. Commun.* **2008**, *1*, 52.

(39) Malmqvist, P.-Å.; Roos, B. O.; Schimmelpfennig, B. *Chem. Phys. Lett.* **2002**, *357*, 230.

(40) Roos, B. O.; Malmqvist, P.-Å. *Phys. Chem. Chem. Phys.* **2004**, *6*, 2919.

(41) Karlström, G.; Lindh, R.; Malmqvist, P.-Å.; Roos, B. O.; Ryde, U.; Veryazov, V.; Widmark, P.-O.; Cossi, M.; Schimmelpfennig, B.; Neogrady, P.; Seijo, L. *Comput. Mater. Sci.* **2003**, *28*, 222.

(42) de Graaf, C.; Sousa, C. *Int. J. Quantum Chem.* **2006**, *106*, 2470.

(43) Petit, S.; Pilet, G.; Luneau, D.; Chibotaru, L.; Ungur, L. *Dalton Trans.* **2007**, 4582.

(44) Chibotaru, L.; Ungur, L.; Aronica, C.; Elmoll, H.; Pilet, G.; Luneau, D. *J. Am. Chem. Soc.* **2008**, *130*, 12445.

(45) Chibotaru, L.; Ungur, L.; Soncini, A. *Angew. Chem., Int. Ed.* **2008**, *47*, 4126.

(46) Soncini, A.; Chibotaru, L. *Phys. Rev. B* **2008**, *77*, 220406.
(47) Maurice, R.; Bastardis, R.; de Graaf, C.; Suaud, N.; Mallah, T.; Guihery, N. *J. Chem. Theory Comput.* **2009**, *5*, 2977.
(48) Maurice, R.; Guihery, N.; Bastardis, R.; de Graaf, C. *J. Chem. Theory Comput.* **2010**, *6*, 55.
(49) Maurice, R.; de Graaf, C.; Guihery, N. *Phys. Rev. B* **2010**, *81*, 214427.
(50) Maurice, R.; de Graaf, C.; Guihery, N. *J. Chem. Phys.* **2010**, *133*, 084307.
(51) Maurice, R.; Pradipto, A. M.; Guihery, N.; Broer, R.; de Graaf, C. *J. Chem. Theory Comput.* **2010**, *6*, 3092.
(52) Gilka, N.; Taylor, P. R.; Marian, C. M. *J. Chem. Phys.* **2008**, *129*, 044102.
(53) Ganyushin, D.; Neese, F. *J. Chem. Phys.* **2008**, *128*, 114117.
(54) Neese, F. *ORCA: An ab Initio, Density Functional and Semiempirical Program Package*; University of Bonn: Bonn, Germany, 2007.
(55) Angeli, C.; Cimiraglia, R.; Evangelisti, S.; Leininger, T.; Malrieu, J.-P. *J. Chem. Phys.* **2001**, *114*, 10252.
(56) Ganyushin, D.; Neese, F. *J. Chem. Phys.* **2006**, *125*, 024103.
(57) Neese, F. *J. Am. Chem. Soc.* **2006**, *128*, 10213.
(58) Neese, F. *J. Chem. Phys.* **2007**, *127*, 164112.
(59) Ganyushin, D.; Gilka, N.; Taylor, P. R.; Marian, C. M.; Neese, F. *J. Chem. Phys.* **2010**, *132*, 144111.
(60) Sinnecker, S.; Neese, F. *J. Phys. Chem. A* **2006**, *110*, 12267.
(61) Duboc, C.; Phoeung, T.; Zein, S.; Pecaut, J.; Collomb, M.-N.; Neese, F. *Inorg. Chem.* **2007**, *46*, 4905.
(62) Ganyushin, D.; Neese, F. *J. Chem. Phys.* **2008**, *128*, 114117.
(63) Zein, S.; Duboc, C.; Lubitz, W.; Neese, F. *Inorg. Chem.* **2008**, *47*, 134.
(64) Zein, S.; Neese, F. *J. Phys. Chem. A* **2008**, *112*, 7976.
(65) Liakos, D. G.; Ganyushin, D.; Neese, F. *Inorg. Chem.* **2009**, *48*, 10572.
(66) Maurice, R.; Sivalingam, K.; Ganyushin, D.; Guihery, N.; de Graaf, C.; Neese, F. *Inorg. Chem.* **2011**, *50*, 6229.
(67) Di Vaira, M.; Orioli, P. L. *Acta Crystallogr., Sect. B: Struct. Crystallogr. Cryst. Chem.* **1968**, *24*, 595. Bertini, I.; Ciampolini, M.; Depporto, P.; Gatteschi, D. *Inorg. Chem.* **1972**, *11*, 2254.
(68) Takahashi, S.; Hill, S. *Rev. Sci. Instrum.* **2005**, *76*, 023114.
(69) Frisch, M. J.; Trucks, G. W.; Schlegel, H. B.; Scuseria, G. E.; Robb, M. A.; Cheeseman, J. R.; Montgomery, Jr., J. A.; Vreven, T.; Kudin, K. N.; Burant, J. C.; Millam, J. M.; Iyengar, S. S.; Tomasi, J.; Barone, V.; Mennucci, B.; Cossi, M.; Scalmani, G.; Rega, N.; Petersson, G. A.; Nakatsuji, H.; Hada, M.; Ehara, M.; Toyota, K.; Fukuda, R.; Hasegawa, J.; Ishida, M.; Nakajima, T.; Honda, Y.; Kitao, O.; Nakai, H.; Klene, M.; Li, X.; Knox, J. E.; Hratchian, H. P.; Cross, J. B.; Bakken, V.; Adamo, C.; Jaramillo, J.; Gomperts, R.; Stratmann, R. E.; Yazyev, O.; Austin, A. J.; Cammi, R.; Pomelli, C.; Ochterski, J. W.; Ayala, P. Y.; Morokuma, K.; Voth, G. A.; Salvador, P.; Dannenberg, J. J.; Zakrzewski, V. G.; Dapprich, S.; Daniels, A. D.; Strain, M. C.; Farkas, O.; Malick, D. K.; Rabuck, A. D.; Raghavachari, K.; Foresman, J. B.; Ortiz, J. V.; Cui, Q.; Baboul, A. G.; Clifford, S.; Cioslowski, J.; Stefanov, B. B.; Liu, G.; Liashenko, A.; Piskorz, P.; Komaromi, I.; Martin, R. L.; Fox, D. J.; Keith, T.; Al-Laham, M. A.; Peng, C. Y.; Nanayakkara, A.; Challacombe, M.; Gill, P. M. W.; Johnson, B.; Chen, W.; Wong, M. W.; Gonzalez, C.; Pople, J. A. *Gaussian 03*, revision D.01; Gaussian, Inc.: Wallingford, CT, 2004.
(70) Hay, P. J.; Wadt, W. R. *J. Chem. Phys.* **1985**, *82*, 299.
(71) Roy, L. E.; Hay, P. J.; Martin, R. L. *J. Chem. Theory Comput.* **2008**, *4*, 1029.
(72) Hay, P. J.; Wadt, W. R. *J. Chem. Phys.* **1985**, *82*, 270.
(73) Krishnan, R.; Binkley, J. S.; Seeger, R.; Pople, J. A. *J. Chem. Phys.* **1980**, *72*, 650. McLean, A. D.; Chandler, G. S. *J. Chem. Phys.* **1980**, *72*, 5639. Curtiss, L. A.; McGrath, M. P.; Blandeau, J.-P.; Davis, N. E.; Binning, R. C.; Radom, L., Jr. *J. Chem. Phys.* **1985**, *103*, 6104.
(74) Hehre, W. J.; Ditchfield, R.; Pople, J. A. *J. Chem. Phys.* **1972**, *56*, 2257. Hariharan, P. C.; Pople, J. A. *Theor. Chim. Acta* **1973**, *28*, 213.
(75) Ditchfield, R.; Hehre, W. J.; Pople, J. A. *J. Chem. Phys.* **1971**, *54*, 724.
(76) Dolg, M.; Wedig, U.; Stoll, H.; Preuss, H. *J. Chem. Phys.* **1987**, *86*, 866.
(77) Martin, J. M. L.; Sundermann, A. *J. Chem. Phys.* **2001**, *114*, 3408.
(78) Dunning, T. H., Jr. *J. Chem. Phys.* **1989**, *90*, 1007.
(79) Due to the ground term degeneracy, it is not possible to optimize the C_3 geometry. Therefore, we have fixed the experimental geometry of all other atoms and relaxed the carbon hydrogen distances for the nondegenerate first excited state. The optimized C−H distances are identical to those obtained for the nondegenerate ground state at the C_1 optimized geometry.
(80) Karlström, G.; Lindh, R.; Malmqvist, P.-Å.; Roos, B. O.; Ryde, U.; Veryazov, V.; Widmark, P.-O.; Cossi, M.; Schimmelpfennig, B.; Neograd, P.; Seijo, L. *Comput. Mater. Sci.* **2003**, *28*, 222.
(81) Anderson, K.; Malmqvist, P.-Å.; Roos, B. O. *J. Chem. Phys.* **1992**, *96*, 1218.
(82) The 15th singlet is very high in energy and is not expected to contribute significantly to the ZFS. Since its reference weight is much lower than the reference weight of the other singlets, it has not been considered in the SO-SI calculation.
(83) Malmqvist, P.-Å.; Roos, B. O. *Chem. Phys. Lett.* **1989**, *155*, 189. Malmqvist, P.-Å.; Roos, B. O.; Schimmelpfennig, B. *Chem. Phys. Lett.* **2002**, *357*, 230.
(84) Roos, B. O.; Lindh, R.; Malmqvist, P.-Å.; Veryazov, V.; Widmark, P. O. *J. Phys. Chem. A* **2005**, *109*, 6575.
(85) Alary, F.; Boggio-Pasqua, M.; Heully, J. L.; Marsden, C. J.; Vicendo, P. *Inorg. Chem.* **2008**, *47*, 5259.
(86) Banci, L.; Benelli, C.; Gatteschi, D. *Inorg. Chem.* **1984**, *23*, 3262.
(87) Abragam, A.; Bleaney, B. *Electron Paramagnetic Resonance of Transition Ions*; Dover Publications: Dover, NY, 1986; p 378.
(88) McGarvey, B. R.; Telser, J. *Inorg. Chem.* **2012**, *51*, 6000.
(89) Bloch, C. *Nucl. Phys.* **1958**, *6*, 329. des Cloizeaux, J. *Nucl. Phys.* **1960**, *20*, 321.